Letter

Evidence for lunar tide effects in Earth's plasmasphere

Chao Xiao [1,11], Fei He [2,11], Quanqi Shi [1] ✉, Wenlong Liu [3,4] ✉, Anmin Tian[1], Ruilong Guo[1], Chao Yue [5], Xuzhi Zhou[5], Yong Wei [2], I. Jonathan Rae[6], Alexander W. Degeling[1], Vassilis Angelopoulos [7], Emmanuel V. Masongsong[7], Ji Liu[8], Qiugang Zong[5], Suiyan Fu[5], Zuyin Pu[5], Xiaoxin Zhang[9], Tieyan Wang[10], Huizi Wang[1] & Zhao Zhang [3,4]

Tides are universal and affect spatially distributed systems, ranging from planetary to galactic scales. In the Earth–Moon system, effects caused by lunar tides were reported in the Earth's crust, oceans, neutral gas-dominated atmosphere (including the ionosphere) and near-ground geomagnetic field. However, whether a lunar tide effect exists in the plasma-dominated regions has not been explored yet. Here we show evidence of a lunar tide-induced signal in the plasmasphere, the inner region of the magnetosphere, which is filled with cold plasma. We obtain these results by analysing variations in the plasmasphere's boundary location over the past four decades from multisatellite observations. The signal possesses distinct diurnal (and monthly) periodicities, which are different from the semidiurnal (and semimonthly) variations dominant in the previously observed lunar tide effects in other regions. These results demonstrate the importance of lunar tidal effects in plasma-dominated regions, influencing understanding of the coupling between the Moon, atmosphere and magnetosphere system through gravity and electromagnetic forces. Furthermore, these findings may have implications for tidal interactions in other two-body celestial systems.

Tides are universal phenomena and often play essential roles in planetary and galactic systems wherever gradients in gravitational attraction are important[1–3]. As the Earth's sole natural satellite, the Moon and its gravitational interaction with Earth have attracted extensive research and curiosity over several hundred years[4]. Periodic lunar tidal effects have been observed in the Earth's crust, oceans, near-ground

geomagnetic field, atmosphere and ionosphere[5–16]. These lunar tides mainly have semidiurnal (and semimonthly) periods[17–21] and are of fundamental importance to conditions on our planet. For example, the Earth's crustal tide can trigger seismic[22–24] and volcanic activity[25], and the ocean tide can influence the flow of heat from equatorial to polar regions[26] and the evolution of primordial terrestrial species from

[1]Chinese Ministry of Education Key Laboratory of Particle Physics and Particle Irradiation, Shandong Provincial Key Laboratory of Optical Astronomy and Solar-Terrestrial Environment, Institute of Space Sciences, School of Space Science and Physics, Shandong University, Weihai, China. [2]Key Laboratory of Earth and Planetary Physics, Institute of Geology and Geophysics, Chinese Academy of Sciences, Beijing, China. [3]School of Space and Environment, Beihang University, Beijing, China. [4]Key Laboratory of Space Environment Monitoring and Information Processing of MIIT, Beihang University, Beijing, China. [5]Institute of Space Physics and Applied Technology, Peking University, Beijing, China. [6]Department of Maths, Physics and Electrical Engineering, Northumbria University, Newcastle, UK. [7]Department of Earth, Planetary, and Space Sciences, Institute of Geophysics and Space Physics, University of California, Los Angeles, CA, USA. [8]Department of Physics, University of Alberta, Edmonton, Alberta, Canada. [9]Key Laboratory of Space Weather, National Center for Space Weather, China Meteorological Administration, Beijing, China. [10]School of Earth Science, Chenggong Campus, Yunnan University, Kunming, China. [11]These authors contributed equally: Chao Xiao, Fei He. ✉e-mail: sqq@sdu.edu.cn; liuwenlong@buaa.edu.cn
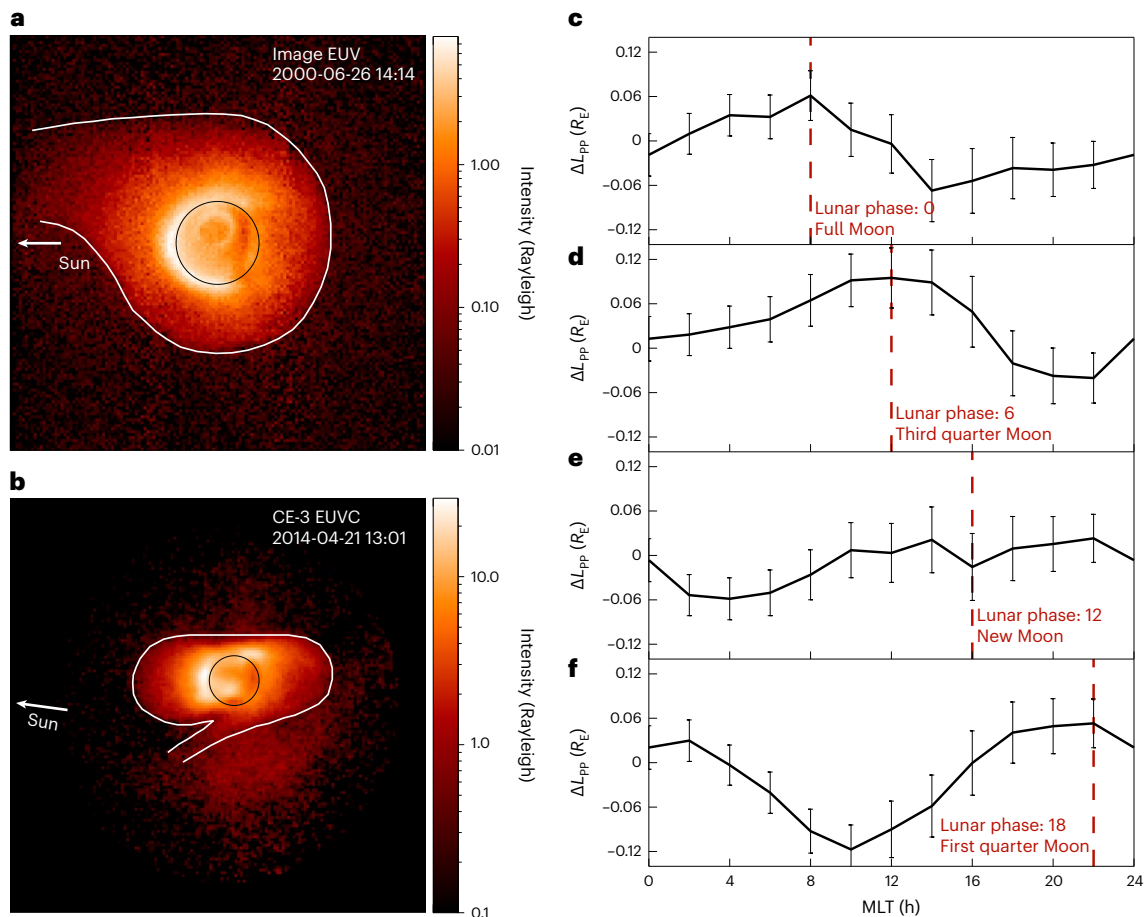
Fig. 1 | Overview of the plasma lunar tide observation in Earth–Moon space. a, A plasmaspheric image taken by the IMAGE EUV imager at 14:14 UT on 26 June 2000 viewed above the Earth's North Pole. **b**, A plasmaspheric image captured by the Chang'e-3 (CE-3) EUV camera at 13:01 UT on 21 April 2014 viewed from the Moon. The EUV emission intensity (in Rayleigh; 1 Rayleigh = 10^6 photons $cm^{-2} s^{-1} sr^{-1}$) is indicated by the colour bars at the right of the panels. A sharp drop in the emission intensity represents the plasmapause as denoted by the white curves. The white arrows indicate the direction of the Sun. The black circles indicate the apparent size of the Earth. **c**, Variations of ΔL_{PP} versus MLT at LP = 0 (full Moon). **d**), Variations of ΔL_{PP} versus MLT at LP = 6 (third quarter Moon). **e**, Variations of ΔL_{PP} versus MLT at LP = 12 (new Moon). **f**, Variations of ΔL_{PP} versus MLT at LP = 18 (first quarter Moon). ΔL_{PP} is plasmapause perturbation data in units of R_E (1 R_E = 6,371 km). The high tide peaks are marked by the red dashed lines. The vertical error bars in panels **c**–**f** denote the 95% confidence intervals.

aquatic life[27]. Atmospheric tides have a global impact on rainfall[28], and ionospheric tides can affect radio transmission and low-Earth-orbit satellite altitude[9,29]. If we follow the four states of matter, they progress from solid, liquid and gas to plasma, which is the dominant component of the Earth–Moon space environment. In the past, lunar tides were mainly found to affect the first three states: solid Earth tides, liquid ocean tides and neutral gas-dominated atmospheric tides. Whether lunar tides can influence the plasma-dominated regions, which are much more extensive in space, has not yet been explored.

The Earth's plasmasphere is the most ideal and representative plasma-dominated place in which to study the existence of lunar tides in plasma, because its basic properties have been studied extensively and there are massive amounts of observational data. The plasmasphere is a collisionless magnetized plasma region that extends along geomagnetic field lines from the upper ionosphere (its source region), filling a roughly torus-shaped volume in near-Earth space. It is composed of cold (1–2 eV) and dense (10^2–10^4 cm^{-3}) plasma with quasi-equal numbers of electrons and ions (~80% H^+, ~10–20% He^+ and ~5–10% O^+), and it plays a key role in particle exchange and storage within the magnetosphere[30,31]. Given its cold, dense plasma properties, the plasmasphere can be regarded as a 'plasma ocean', and the plasmapause represents the 'surface' of this ocean because of the dramatic change of plasma

properties across this boundary. The location of the plasmapause is thus an important parameter in the study of plasma dynamics within the inner magnetosphere[32–35].

Previous studies have shown that the plasmapause location reflects the dynamics of the entire cold plasma, which can strongly affect energetic particle distributions in the inner magnetosphere by significantly influencing the excitation and propagation of electromagnetic waves, and subsequently impact radiation belt and ring current dynamics[36–38]. Hence, to explore the existence of a lunar tidal effect in this cold plasma ocean, it is natural to examine whether these 'sea surface' variations may be associated with the lunar cycle. Figure 1a,b shows two typical satellite images of the plasmasphere obtained by the Extreme Ultraviolet (EUV) imager on board NASA's Imager for Magnetosphere-to-Aurora Global Exploration (IMAGE) spacecraft in polar perspective and the EUV camera aboard China's Chang'e-3 lunar lander in lunar perspective, respectively, with corresponding plasmapause outlines indicated by white curves. The findings reported in this article demonstrate a significant lunar tidal effect in the plasmapause location, providing a causal link by which the Moon exerts an influence on magnetospheric dynamics. This expands our understanding of Earth–Moon interactions in a direction that has not been previously considered, and provides important clues for future investigations
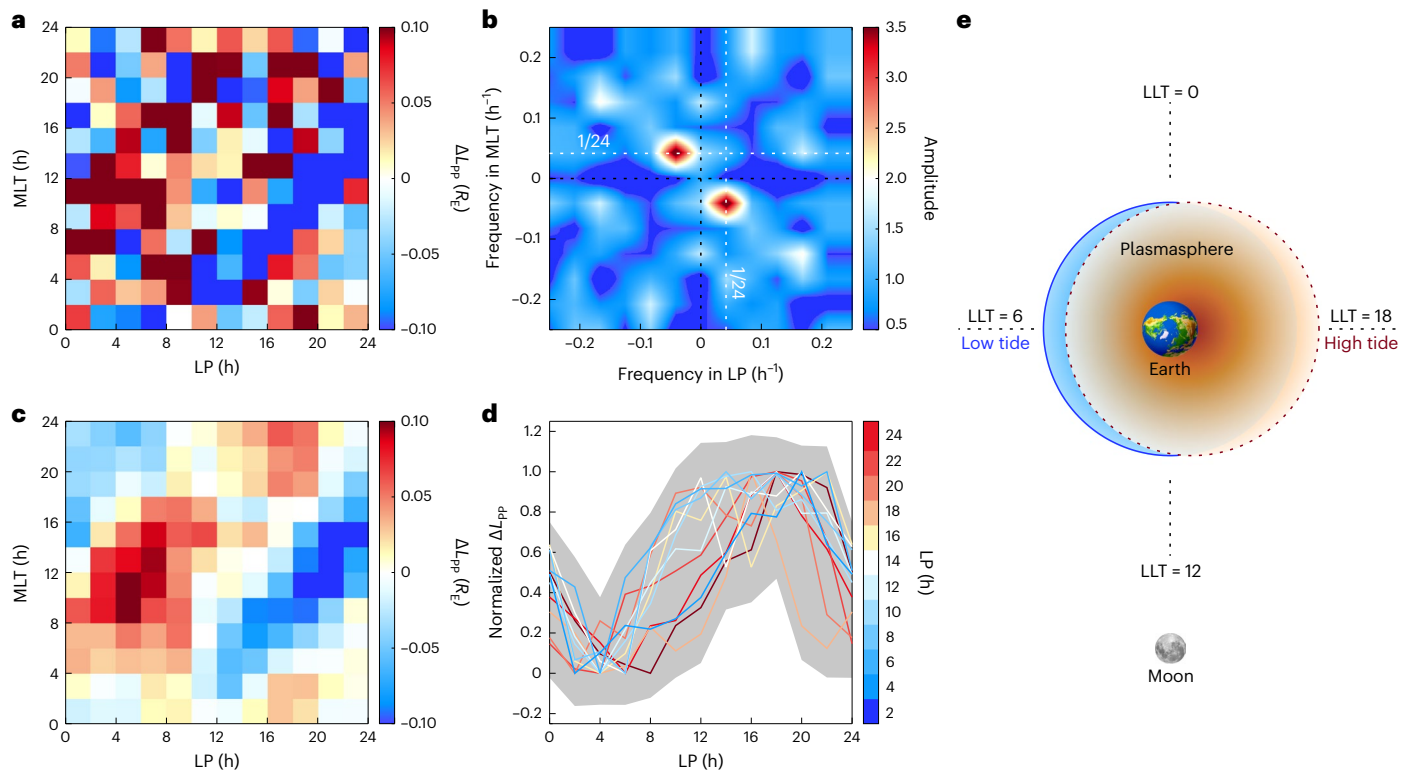
Fig. 2 | The characteristics of LTWP. a, The variation of ΔL_{PP} binned in 2 h windows in both MLT and LP, where ΔL_{PP} is plasmapause perturbation data in units of R_E. **b**, The two-dimensional discrete Fourier transform amplitude of ΔL_{PP} in **a**. The two red spots represent frequencies with the highest amplitude in MLT and LP, respectively. The black and white dashed lines indicate frequencies equal to 0 and 1/24 for reference, respectively. **c**, The variation of ΔL_{PP} binned in 6 h windows in both MLT and LP. **d**, Variations of the normalization of **c** as a function of LLT at different LPs. The LLT is defined as (12 − LP + MLT) mod 24 with LLT = 12

corresponding to lunar noon. Detailed definitions of MLT, LP and LLT can also be found in the Methods and Extended Data Fig. 4. The grey shaded band represents the normalized 95% confidence interval error, which is defined here as the 95% confidence interval error divided by the difference between the maximum and the minimum of ΔL_{PP}. **e**, Illustration of the LWTP in the LLT frame in the Earth–Moon space. The background plasmapause is shown by the blue circle. The modulation of the plasmapause by lunar tide is shown by the red dashed circle; left for low tide and right for high tide.

in broader regions and two-body celestial systems, including other planetary systems in our solar system and beyond.

A large database of plasmapause positions[35] determined by 50,778 plasmapause crossings from the Time History of Events and Macroscale Interactions during Substorms (THEMIS) mission and other missions is used in this study (the largest such database compiled to date, detailed in the Methods, and examples of THEMIS and Cluster plasmapause crossings are shown in Extended Data Fig. 1). The survey period is from November 1977 to December 2015, covering almost four solar cycles (21, 22, 23 and 24). This provides a unique opportunity to study lunar influences on plasmapause position by eliminating external factors, such as effects from solar activity. In this investigation, 35,982 (~71% of the total) in situ plasmapause crossings under low-activity geomagnetic conditions (Dst > −50 nT, AE < 300 nT and Kp ≤ 3, where Dst is the disturbance-storm-time index, AE is the aurora electrojet index and Kp is the 3-hour averaged geomagnetic activity index, respectively.) were selected to reduce the possible effects of varying solar wind and geomagnetic activity and minimize statistical uncertainties. To extract the lunar tide signal, a database of plasmapause perturbations categorized by lunar phase (LP) was compiled and used for the following investigations (Methods and Extended Data Figs. 2 and 3).

Figures 1 and 2 show conclusive evidence of a lunar tidal effect on the plasmapause location. For convenience in this study, LP is defined as the magnetic local time (MLT) of lunar position (Extended Data Fig. 4). Figure 1c–f shows the perturbations in plasmapause position as a function of MLT for LP of 0 h (full Moon), 6 h (third quarter Moon), 12 h (new Moon) and 18 h (first quarter Moon), respectively. These

panels reveal that the high tide peaks (marked by red dashed lines) of the perturbations progress regularly with LP, and the MLT (longitude) of the high tide bulges is ~6 h (90°) ahead of the LP. This is further demonstrated below in detail. The plasmapause perturbation data (ΔL_{PP}) was binned in 2 h windows in both MLT and LP, and the resulting two-dimensional distribution of average values in each bin is shown in Fig. 2a. Figure 2b shows the two-dimensional discrete Fourier transform[39] amplitude of this dataset, which unambiguously illustrates the diurnal and monthly (lunar cycle) variations. Figure 2c depicts the distribution of ΔL_{PP} binned in 6 h windows in both MLT and LP, more clearly showing the existence of lunar tides in the plasmasphere, hereafter referred to as lunar tidal wave in the plasmapause (LTWP). Since there is only one high tide and one low tide for each MLT or LP, the period of LTWP is diurnal and monthly, contrasting with most of the previously observed lunar tides in other regions of the Earth system, which have predominantly semidiurnal and semimonthly periods[40]. It is also clearly shown in Fig. 2c that the MLT of the high tide is about 6 h ahead of the LP (longitude difference ~90°)—that is, they have a well-defined linear relationship that is expressed by MLT of the high tide = (0.956 ± 0.051) × LP + 6.336 ± 1.29. Given the clear synchronization with LP, it is logical to define a local time coordinate with respect to lunar (instead of solar) position, which we label lunar local time (LLT; with 12 h corresponding to lunar zenith, as illustrated in Fig. 2e). Figure 2d depicts LLT variations of the normalized perturbations in plasmapause position for each LP. As shown in Fig. 2c, the amplitude of ΔL_{PP} is ±0.13 Earth radii (R_E). These three panels clearly show the features of the lunar tide in the plasmasphere: the high tide (maximum of about 0.12R_E) occurs at LLT = 18 h,
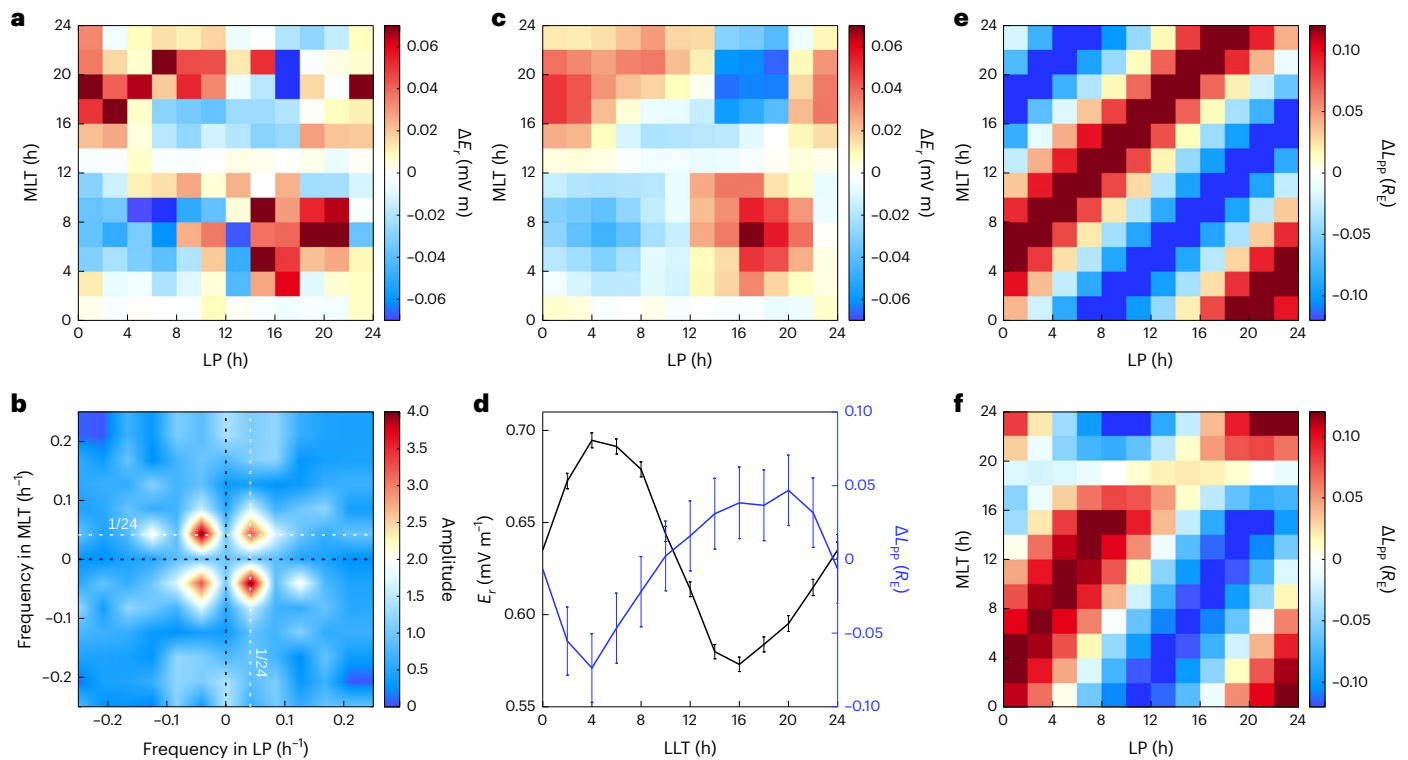
Fig. 3 | Independent electric field observation and cold plasma convection modelling. a, The perturbations (ΔE_r) of the radial component of the electric field E_r (positive E_r towards the Earth in this paper) measured by the Van Allen Probes binned in 2 h windows in both MLT and LP. **b**, The two-dimensional discrete Fourier transform amplitude of ΔE_r in **a**. The black and white dashed lines indicate frequencies equal to 0 and 1/24 for reference, respectively.

c, The perturbations of ΔE_r binned in 6 h windows in both MLT and LP.
d, Variations of E_r (black) and ΔL_{PP} (blue) with LLT, where ΔL_{PP} is plasmapause perturbation data in units of R_E. The vertical error bars in panel **d** denote the 95% confidence intervals. **e**,**f**, Perturbations of the plasmapause derived from the two plasmapause formation models, zero parallel force (ZPF) surface (**e**) and LCE (**f**).

while the low tide (minimum of about $-0.14 R_E$) occurs at LLT = 6 h, as illustrated in Fig. 2e.

To rule out the possibility of data anomalies and ensure the reliability of the results, the database is divided into two subdatasets in three different ways. In all cases, similar tidal signals are observed (Methods and Extended Data Figs. 5–7). We have made a video showing tidal changes at the plasmapause related to LP (Supplementary Video 1). It is worth noting that because the plasmapause location has also been found to be modulated by solar rotation (for example, corotating interaction regions) with a period of about 27 days[41], one could reasonably suspect that the signal we are observing is in fact modulated by the Sun. However, our use of low geomagnetic activity data with a long-term average and the strong correlation of the high tide of LTWP with the LP rules out the possibility of the solar rotation effect for this signal.

The essential question now is how does such a lunar tide with diurnal and monthly periods occur in the plasmasphere? The motion of the cold plasma in the plasmasphere is primarily subject to $\mathbf{E} \times \mathbf{B}$ drift (where $\mathbf{E}$ is electric field and $\mathbf{B}$ is magnetic field) and thus the electric field is essential in determining the position of the plasmapause. The electric field in the inner magnetosphere is composed of the steady corotation electric field ($\mathbf{E}_{coro}$) that is determined by Earth's magnetic moment and rotation, and the varying magnetospheric convection electric field ($\mathbf{E}_{conv}$) that is controlled by solar wind and geomagnetic activity. Figure 3a shows the perturbations (ΔE_r) of the radial component of the electric field E_r (positive E_r towards the Earth) measured by the Van Allen Probes (Methods) binned in 2 h windows in both MLT and LP, with the corresponding amplitude of its two-dimensional discrete Fourier transform shown in Fig. 3b. Both diurnal and monthly variations are clearly apparent in these plots, similar to the case for ΔL_{PP}. Figure 3c

shows ΔE_r binned in 6 h windows in both MLT and LP, which more clearly shows the existence of a similar tidal disturbance in the electric field. Figure 3d shows variations of E_r with LLT, which varies from 0.57 to 0.69 mV m^{-1}. The maximum (minimum) E_r occurs at LLT = 6 (18) h, which is opposite to LTWP (blue line in Fig. 3d). There is a strong negative correlation between the mean values of LTWP and E_r for each sector with a correlation coefficient of −0.94. By subtracting the baseline of the E_r (0.63 mV m^{-1}, which agrees well with the averaged corotation electric field of 0.61 mV m^{-1} over the range of L values (McIlwain L, corresponding to the equatorial radius of a drift shell of a charged particle)[42] from 3 to 6) in Fig. 3d, ΔE_r is obtained and fitted by the function $\Delta E_r = (0.0155 \pm 0.0022) \times \cos((0.2618 \pm 0.0002) \times LLT) + (0.0578 \pm 0.0012) \times \sin((0.2618 \pm 0.0002) \times LLT)$ with a correlation coefficient of 0.99.

Subsequently, models for plasmapause formation are considered to evaluate whether such an electric field perturbation is consistent with and can reproduce the observed LTWP. One model is based on the kinetic theory of plasmapause formation (that is, via the physical process of interchange motion, driven unstable at the location where the Roche limit surface or ZPF surface, which becomes tangential to the magnetospheric convection-corotation streamlines)[43–46]. The simulated ΔL_{PP} in Fig. 3e demonstrates that this model can successfully reproduce this tidal phenomenon (Methods). The correlation coefficient between observed and simulated ΔL_{PP} is about 0.70, and the ΔL_{PP} (approximately -0.15–$0.14 R_E$) obtained from the model agrees well with the observations (-0.14–$0.12 R_E$). Another model considers that the plasmapause coincides with the last closed equipotential (LCE) of the magnetospheric convection electric field, and thus it is called the LCE model[47]. This model is suggested to work under quiet or quasi-static geomagnetic conditions[30]. In our study, we apply this model with the limitation of Kp = 3. It is found that LTWP can

be qualitatively reproduced with a 38% downscaling of observed ΔE_r (Fig. 3f and Methods).

Therefore, both observations and model simulations suggest that the perturbations of plasmapause position result from the disturbed radial electric field. Understanding the causal link between the LP and the perturbed electric field is a subject of ongoing research. One possibility is that the neutral winds in the ionosphere, which are modulated by LP, can generate an electric potential difference that can be mapped along field lines threading the plasmasphere and perturb the radial electric field that modulates the plasmapause position. Preliminary model calculations support this hypothesis and will be further developed.

Another possible origin of the observed lunar tidal signal might be the Moon's gravitational field perturbation on the ZPF surface, since the position and shape of the virtual ZPF depend on the field-aligned component of the Earth's gravitational field. However, including the Moon's gravitational effect in the ZPF theory just introduces a very small extra perturbation of -0.01% on the plasmapause position (Methods), and thus is negligible.

Our discovery of this plasma tidal effect with distinct characteristics may indicate a fundamental interaction mechanism in the Earth–Moon system that has not been previously considered. Furthermore, reflected by this plasma tide, the plasma flow in the entire Earth–Moon space exists as a persistent background variation of the magnetosphere and can modulate Earth–Moon space dynamics continuously, although the observed perturbations caused by the lunar tide are often relatively small compared to those arising from solar activity. Since this plasma tide effect appears to be predictably fundamental, it may be expected not only in the plasmasphere, but over a much wider set of phenomena. For example, plasmapause surface waves can alter energy transport from the magnetosphere to the upper atmosphere[48], while whistler mode chorus and hiss waves, and also electromagnetic ion cyclotron waves near the plasmapause contribute significantly to electron acceleration and loss in the Van Allen radiation belt[49,50]. We suspect that the observed plasma tide may subtly affect the distribution of energetic radiation belt particles, which are a well-known hazard to space-based infrastructure and human activities in space. It is therefore worthwhile to look for evidence of this effect in future studies—for example, by checking for correlations of variations in the distribution of 'zebra stripes'[51] with LP. These have been suggested to be formed by a weak electric field independent of corotation[52]; however, the observed electric field modulated by this lunar plasma tide may contribute. As for how the LP adjusts the radial electric field, we suspect that the Moon may modulate the radial electric field by affecting the upper atmosphere.

Whether the magnetic field or plasma lunar tides seen in space are related to the Earth's crustal and oceanic tide[53] is also a question worthy of discussion. The configuration and structure of Earth's cold plasma in relation to the magnetosphere is not unique to the Earth, and similar structures have been found at other planets[54–56] and astrophysical objects[57]. Here, we can summarize that the three fundamental elements necessary for this plasma tidal signal are the existence of a two-body celestial system, plasma and a magnetic field. Because the planetary environments in the stellar system that meet all these conditions are very common, this plasma tide may be observed universally throughout the cosmos. Therefore, the finding of this lunar tidal effect in the plasmasphere not only extends our knowledge of the Earth–Moon system, but also open new perspectives for further studies of tidal interactions in other planetary and larger-scale systems.

Online content

References

1. Renaud, F., Boily, C. M., Naab, T. & Theis, C. Fully compressive tides in galaxy mergers. *Astrophys. J.* **706**, 67–82 (2009).
2. Ivanov, P. B. & Papaloizou, J. C. B. Dynamic tides in rotating objects: orbital circularization of extrasolar planets for realistic planet models. *Mon. Notices Royal Astron. Soc.* **376**, 682–704 (2007).
3. Fouchard, M., Froeschlé, C., Valsecchi, G. & Rickman, H. Long-term effects of the galactic tide on cometary dynamics. *Celest. Mech. Dyn. Astron.* **95**, 299–326 (2006).
4. Cartwright, D. E. *Tides: A Scientific History* (Cambridge Univ. Press, 1999).
5. Matsushita, S. in *Geophysik III [Geophysics III]* Handbuch der Physik [Encyclopedia of Physics] (ed. Bartels, J.) 547–602 (Springer, 1967); https://doi.org/10.1007/978-3-642-46082-1_2
6. Forbes, J. M., Zhang, X., Bruinsma, S. & Oberheide, J. Lunar semidiurnal tide in the thermosphere under solar minimum conditions. *J. Geophys. Res. Space Phys.* **118**, 1788–1801 (2013).
7. Niu, X. et al. Lunar tidal winds in the mesosphere over Wuhan and Adelaide. *Adv. Space Res.* **36**, 2218–2222 (2005).
8. Paulino, A. R., Batista, P. P. & Batista, I. S. A global view of the atmospheric lunar semidiurnal tide. *J. Geophys. Res. Atmos.* **118**, 13128–13139 (2013).
9. Pedatella, N. M. & Forbes, J. M. Global structure of the lunar tide in ionospheric total electron content. *Geophys. Res. Lett.* **37**, L06103 (2010).
10. Sakazaki, T. & Hamilton, K. Discovery of a lunar air temperature tide over the ocean: a diagnostic of air-sea coupling. *npj Clim. Atmos. Sci.* **1**, 25 (2018).
11. Stening, R. J., Tsuda, T. & Nakamura, T. Lunar tidal winds in the upper atmosphere over Jakarta. *J. Geophys. Res. Space Phys.* **108**, 1192 (2003).
12. Yamazaki, Y., Richmond, A. D. & Yumoto, K. Stratospheric warmings and the geomagnetic lunar tide: 1958-2007. *J. Geophys. Res. Space Phys.* **117**, A04301 (2012).
13. Zhang, J. T., Forbes, J. M., Zhang, C. H., Doornbos, E. & Bruinsma, S. L. Lunar tide contribution to thermosphere weather. *Space Weather* **12**, 538–551 (2014).
14. Fejer, B. G. et al. Lunar-dependent equatorial ionospheric electrodynamic effects during sudden stratospheric warmings. *J. Geophys. Res. Space Phys.* **115**, A00G03 (2010).
15. Li, N. et al. Responses of the ionosphere and neutral winds in the mesosphere and lower thermosphere in the Asian-Australian sector to the 2019 southern hemisphere sudden stratospheric warming. *J. Geophys. Res. Space Phys.* **126**, e2020JA028653 (2021).
16. Owolabi, C. et al. Investigation on the variability of the geomagnetic daily current during sudden stratospheric warmings. *J. Geophys. Res. Space Phys.* **124**, 6156–6172 (2019).
17. Mo, X. H. & Zhang, D. H. Lunar tidal modulation of periodic meridional movement of equatorial ionization anomaly crest during sudden stratospheric warming. *J. Geophys. Res. Space Phys.* **123**, 1488–1499 (2018).
18. Sabaka, T. J., Tyler, R. H. & Olsen, N. Extracting ocean-generated tidal magnetic signals from Swarm data through satellite gradiometry. *Geophys. Res. Lett.* **43**, 3237–3245 (2016).
19. Park, J., Lühr, H., Kunze, M., Fejer, B. G. & Min, K. W. Effect of sudden stratospheric warming on lunar tidal modulation of the equatorial electrojet. *J. Geophys. Res. Space Phys.* **117**, A03306 (2012).
20. Pedatella, N. M., Liu, H.-L., Richmond, A. D., Maute, A. & Fang, T.-W. Simulations of solar and lunar tidal variability in the mesosphere and lower thermosphere during sudden stratosphere warmings and their influence on the low-latitude ionosphere. *J. Geophys. Res. Space Phys.* **117**, A08326 (2012).

21. Liu, J., Zhang, D., Hao, Y. & Xiao, Z. Multi-instrumental observations of the quasi-16-day variations from the lower thermosphere to the topside ionosphere in the low-latitude eastern Asian sector during the 2017 sudden stratospheric warming event. *J. Geophys. Res. Space Phys.* **125**, e2019JA027505 (2020).

22. Cochran, E. S., Vidale, J. E. & Tanaka, S. Earth tides can trigger shallow thrust fault earthquakes. *Science* **306**, 1164–1166 (2004).

23. Heaton, T. H. Tidal triggering of earthquakes. *Geophys. J. Int.* **43**, 307–326 (1975).

24. Tolstoy, M., Vernon, F. L., Orcutt, J. A. & Wyatt, F. K. Breathing of the seafloor: tidal correlations of seismicity at axial volcano. *Geology* **30**, 503–506 (2002).

25. Kasahara, J. Tides, earthquakes, and volcanoes. *Science* **297**, 348–349 (2002).

26. Green, J. A. M. & Huber, M. Tidal dissipation in the early Eocene and implications for ocean mixing. *Geophys. Res. Lett.* **40**, 2707–2713 (2013).

27. Palmer, J. D. *The Biological Rhythms and Clocks of Intertidal Animals* (Oxford Univ. Press, 1995).

28. Kohyama, T. & Wallace, J. M. Rainfall variations induced by the lunar gravitational atmospheric tide and their implications for the relationship between tropical rainfall and humidity. *Geophys. Res. Lett.* **43**, 918–923 (2016).

29. Wu, T., Liu, J., Lin, C. & Chang, L. C. Response of ionospheric equatorial ionization crests to lunar phase. *Geophys. Res. Lett.* **47**, e2019GL086862 (2020).

30. Lemaire, J. F., Gringauz, K. I., Carpenter, D. L. & Bassolo, V. *The Earth's Plasmasphere* (Cambridge Univ. Press, 1998); https://doi.org/10.1017/CBO9780511600098

31. Zhou, X. et al. On the formation of wedge-like ion spectral structures in the nightside inner magnetosphere. *J. Geophys. Res. Space Phys.* **125**, e2020JA028420 (2020).

32. Liu, W. et al. Poloidal ULF wave observed in the plasmasphere boundary layer. *J. Geophys. Res. Space Phys.* **118**, 4298–4307 (2013).

33. Liu, X. et al. Dynamic plasmapause model based on THEMIS measurements. *J. Geophys. Res. Space Phys.* **120**, 10543–10556 (2015).

34. He, F. et al. A new solar wind-driven global dynamic plasmapause model: 2. Model and validation. *J. Geophys. Res. Space. Phys.* **122**, 7172–7187 (2017).

35. Zhang, X. et al. A new solar wind-driven global dynamic plasmapause model: 1. Database and statistics. *J. Geophys. Res. Space Phys.* **122**, 7153–7171 (2017).

36. Li, X., Baker, D. N., O'Brien, T. P., Xie, L. & Zong, Q. G. Correlation between the inner edge of outer radiation belt electrons and the innermost plasmapause location. *Geophys. Res. Lett.* **33**, L14107 (2006).

37. Cao, J. B. et al. First results of low frequency electromagnetic wave detector of TC-2/Double Star program. *Ann. Geophys.* **23**, 2803–2811 (2005).

38. Lorentzen, K. R., Blake, J. B., Inan, U. S. & Bortnik, J. Observations of relativistic electron microbursts in association with VLF chorus. *J. Geophys. Res. Space Phys.* **106**, 6017–6027 (2001).

39. Rao, K. R., Kim, D. N. & Hwang, J. J. (2010) Two-Dimensional Discrete Fourier Transform. In: (Rao, K. R., Kim, D. N. & Hwang, J. J. (eds) *Fast Fourier Transform – Algorithms and Applications*. Springer, Heidelberg, pp 127–184. https://doi.org/10.1007/978-1-4020-6629-0_5

40. Forbes, J. M. & Zhang, X. Lunar tide in the F region ionosphere. *J. Geophys. Res. Space Phys.* **124**, 7654–7669 (2019).

41. Thaller, S. A. et al. Solar rotation period driven modulations of plasmaspheric density and convective electric field in the inner magnetosphere. *J. Geophys. Res. Space Phys.* **124**, 1726–1737 (2019).

42. McIlwain, C. E. Coordinates for mapping the distribution of magnetically trapped particles. *J. Geophys. Res.* **66**, 3681–3691 (1961).

43. Lemaire, J. The 'Roche-limit' of ionospheric plasma and the formation of the plasmapause. *Planet. Space Sci.* **22**, 757–766 (1974).

44. Lemaire, J. The mechanics of formation of the plasmapause. *Ann. Geophys.* **31**, 175–189 (1975).

45. Lemaire, J. The plasmapause formation. *Phys. Scr.* **T18**, 111–118 (1987).

46. Lemaire, J. Differential drift of plasma clouds in the magnetosphere: an update. *J. Atmos. Sol. Terr. Phys.* **63**, 1281–1284 (2001).

47. Brice, N. M. Bulk motion of the magnetosphere. *J. Geophys. Res.* **72**, 5193–5211 (1967).

48. He, F. et al. Plasmapause surface wave oscillates the magnetosphere and diffuse aurora. *Nat. Commun.* **11**, 1668 (2020).

49. Summers, D., Ni, B. & Meredith, N. P. Timescales for radiation belt electron acceleration and loss due to resonant wave-particle interactions: 2. Evaluation for VLF chorus, ELF hiss, and electromagnetic ion cyclotron waves. *J. Geophys. Res. Space Phys.* **112**, A04207 (2007).

50. Miyoshi, Y. et al. Precipitation of radiation belt electrons by EMIC waves, observed from ground and space. *Geophys. Res. Lett.* **35**, L23101 (2008).

51. Ukhorskiy, A. Y. et al. Rotationally driven 'zebra stripes' in Earth's inner radiation belt. *Nature* **507**, 338–340 (2014).

52. Liu, Y., Zong, Q.-G., Zhou, X.-Z., Foster, J. C. & Rankin, R. Structure and evolution of electron 'zebra stripes' in the inner radiation belt. *J. Geophys. Res. Space Phys.* **121**, 4145–4157 (2016).

53. Gallego, A. et al. Tidal modulation of continuous nonvolcanic seismic tremor in the Chile triple junction region. *Geochem, Geophys. Geosyst.* **14**, 851–863 (2013).

54. Nimmo, F. & Pappalardo, R. T. Diapir-induced reorientation of Saturn's moon Enceladus. *Nature* **441**, 614–616 (2006).

55. Lainey, V., Arlot, J.-E., Karatekin, Ö. & Van Hoolst, T. Strong tidal dissipation in Io and Jupiter from astrometric observations. *Nature* **459**, 957–959 (2009).

56. Bagheri, A., Khan, A., Efroimsky, M., Kruglyakov, M. & Giardini, D. Dynamical evidence for Phobos and Deimos as remnants of a disrupted common progenitor. *Nat. Astron.* **5**, 539–543 (2021).

57. Bagenal, F. Giant planet magnetospheres. *Annu. Rev. Earth Planet. Sci.* **20**, 289–328 (1992).

Methods

Plasmapause database

The compilation of the plasmapause database is detailed in ref. [35]. Here we briefly introduce the data sources and plasmapause determination methods. According to different satellite observation datasets, a variety of plasmapause determination methods have been developed. For the THEMIS and Polar satellites, the spacecraft potential (that is, the electric potential of the spacecraft body relative to the ambient plasma) and the electron thermal velocity are used to calculate the electron density. A detailed introduction of this method is given in ref. [58] and ref. [59]. The estimated error (a factor of 2) of this method is smaller than the typical density changes across the plasmapause, thus this method has been widely used to determine plasmapause positions[60,61]. An example of the satellite potential and corresponding electron density measured by THEMIS is shown in Extended Data Fig. 1a,b. For the plasma wave instruments of various satellite missions (for example, International Sun–Earth Explorer-1, Plasma Wave Instrument of Dynamics Explorer 1, Plasma Wave and Sounder of Akebono, Plasma Wave Experiment of Combined Release and Radiation Effects Satellite, Plasma Wave Instrument of Polar, Radio Plasma Imager of IMAGE, Waves of High Frequency and Sounder for Probing of Density by Relaxation of Cluster, and Electric and Magnetic Field Instrument Suite and Integrated Science of Van Allen Probes), the electron density (n_e (cm^{-3})) is given by $n_e = (f^2_{UHR} - f^2_{ce})/8{,}980^2$, where f_{UHR} is the upper hybrid resonance frequency, $f_{ce} = eB/m_e$ is the electron cyclotron frequency, e is the electron charge magnitude, B is the strength of the magnetic field and m_e is the electron mass[62]. Since some satellites are not equipped with a magnetometer, B is obtained by the Tsyganenko 2007 external magnetic field model combined with the International Geomagnetic Reference Field internal magnetic field model[63,64]. In terms of deducing electron densities by the plasma wave instruments, this method has been proven to be very successful in many studies[62,65–68]. Extended Data Figure 1c,d illustrates a corresponding example of the spectrogram of the plasma waves measured by Cluster-4 and the electron density deduced from the upper hybrid resonance frequency from 02:00 universal time (UT) to 03:30 UT on 25 January 2002. The criterion for identifying the plasmapause adopted in previous studies and used in this investigation is that the electron density changes by a factor of five or more within a short distance of ~0.5R_E. Based on this criterion, the black vertical dashed lines mark the plasmapause position.

Plasmapause perturbations at different LP

To extract the lunar tide signal in the plasmapause positions, the averaged background profile of the plasmapause is constructed with the following steps. The MLT is divided into 241 bins with intervals of 0.1 h, and the average position of the plasmapause in each bin is calculated to obtain the averaged background profile of the plasmapause. This profile is subtracted from the plasmapause positions. Through this process, the dawn–dusk asymmetry and geomagnetic activity-induced variations of the plasmapause are almost eliminated. A database of plasmapause perturbations as a function of LP is formed and used for the following investigations.

Statistical uncertainty considerations and data processing

Although the database contains 35,982 plasmapause crossings, we need to divide these events into several bins in MLT and LP phase, to explore the possibility of a lunar tide signal (for example, we use 12 bins each—that is, MLT = 2:2:24 h and LP = 2:2:24 h, respectively). This reduces the level of confidence we can assert for the mean values of plasmapause location for each bin, due to the lower number of counts.

Extended Data Figure 2a shows the distribution of perturbations in plasmapause radial distance in the MLT–LP frame, ranging from −0.3 to 0.3R_E. Extended Data Figure 2b shows the corresponding 95% confidence interval (ranging from 0.05 to 0.2R_E, and higher on the dusk side

due to plasmapause variations associated with evolving plasmaspheric plume structures, as shown in Fig. 1a,b). At first glance, Extended Data Fig. 2a appears to be dominated by random fluctuations in the range of ±0.3R_E; however, a low-frequency underlying signal is also discernible. Given that these fluctuations are of the same order as the confidence interval, we apply spatial smoothing or low-pass filtering to enhance the underlying signal.

It is important to note that the smoothing window size within a period of an oscillatory signal does not change its periodic nature (although it can reduce its amplitude). Extended Data Figure 3a shows a simple example in which a sine function with added noise is smoothed using different smoothing windows. The function is $y = \sin(x) + \mathrm{rand}(-1, 1)$, where rand(−1, 1) represents a random number between −1 and 1. Its period is 2π and the data within a period ($0 \le x \le 2\pi$) is shown in the figure by a black line. The red, green, blue and yellow lines represent the results of smoothing with a window size equal to $1/4\pi$, $1/2\pi$, $3/4\pi$ and π, respectively. It is shown that these smoothed results can more clearly display the changing trend of the data without changing the period of the data, but the amplitude of the data will decrease with the increasing size of the smoothing window.

Extended Data Fig. 3b–e shows the distribution of perturbations of plasmapause position in the MLT–LP frame with smoothing window equal to 3, 6, 9 and 12 h, respectively. We obtain a clear lunar tidal signal, which has diurnal (and monthly) periodicities, and this lunar signal becomes clearer as the smoothing window is increased. Therefore, to obtain clear results (accurate period and amplitude), we chose 6 h (a quarter of a period) for the smoothing window in this study.

Descriptions of MLT, LP and LLT

The MLT, LP and LLT variables all refer to spatial, azimuthal locations and are defined in Extended Data Fig. 4. The MLT is usually used to define azimuthal locations in the Sun–Earth reference frame. When looking from the North Pole, the MLT increases anticlockwise from 0 at midnight to 6 at dawn, 12 at noon, 18 at dusk and 24 at midnight. For convenience in this study, the LP is defined as the MLT of the lunar position with LP values of 0/24, 6, 12 and 18 corresponding to the full Moon, third quarter Moon, new Moon and first quarter Moon, respectively. The LLT is based on the MLT defined with respect to the Moon (instead of the Sun). LLT is always equal to 0 along the magnetic meridian intersecting the far side of the Earth–Moon line, and is always equal to 12 along the magnetic meridian intersecting the near side of the Earth–Moon line. For an azimuthal location P at MLT in Earth's frame, when the Moon is at LP, the corresponding LLT is defined as (12 − LP + MLT) mod 24.

Van Allen Probes observations of radial electric field

In this study, the electric field data measured by the Van Allen Probes satellites between L values of 3–6 from January 2013 to May 2019 were used. The sensitivity of the Electric Fields and Waves instrument on board the Van Allen Probes is 0.1 mV m^{-1} or 10% of the amplitude[69–71]. Note that for Van Allen Probes spacecraft, the electric field component (E_x) along the spin axis is estimated using the assumption that $\mathbf{E} \cdot \mathbf{B} = 0$ or the parallel electric field is zero under the conditions of $|B_y/B_x| < 4$ and $|B_z/B_x| < 4$. To obtain electric field data near the magnetic equator, we selected the electric field data within the magnetic latitude range between −15° and 15° and take its radial component to obtain observations of variations in E_r with LLT. Here, the size of the smoothing window is 6 h; for example, LLT = 6 stands for 3 < LLT < 9. The method used to determine ΔE_r is similar to the method of obtaining the ΔL_{PP}—that is, the MLT is divided into 240 bins with intervals of 0.1 h, and the average radial component of the observed magnetospheric electric field (E_r) in each bin is calculated to obtain the averaged background profile of the E_r, and the perturbations (ΔE_r) of the E_r equal to E_r minus its interpolated background profile.

Including the disturbed electric field in plasmapause formation models

Since the motion of plasma in the plasmasphere is mainly controlled by the $\mathbf{E} \times \mathbf{B}$ drift, the configuration of the plasmasphere is primarily determined by the electric field, assuming a steady magnetic field. Accordingly, the electric field is assumed to be electrostatic (curl-free) and contains two parts. The first is $\mathbf{E}_{coro}$, calculated from the differentiation of the corotation potential[72] $\Phi_C = -\Omega_E \mu M_E/(4\pi L R_E)$, where Ω_E is the rotation speed of the Earth, μ is the magnetic permeability, M_E is the magnetic moment of the Earth's dipole and L denotes the L value. The second is $\mathbf{E}_{conv}$, which is calculated with the Volland–Stern potential model[73,74]. Plasmapause formation models are adopted to verify whether the LTWP is generated by the lunar-tide-inducing electric field perturbations.

One model is based on the ZPF theory[30]. In this theory, the plasmapause position is expressed by $L_{PP} = (2GM/3\Omega^2 R_E{}^3)^{1/3} = (2GM/3R_E{}^3)^{1/3}\Omega^{-2/3}$, where M is the mass of the Earth, G is the universal gravitational constant, R_E is the Earth's radius and Ω is the cold plasma angular velocity. The ZPF theory involves consideration of gravitation on cold plasma along magnetic field lines in the frame rotating with angular speed Ω. The above result is calculated for the case of the Earth in isolation. We therefore check whether the addition of lunar gravitation in this formulation can directly provide a perturbation to L_{PP} that would explain the observed variations with LP. This results in a cubic equation for L_{PP}, given by $L_{PP}{}^3 - (2GM/3\Omega^2 R_E{}^3)(1 - (M_m L_{PP}{}^2/ML_m{}^2)\cos\varphi) = 0 + O((L_{PP}/L_m)^3)$, where M_m is the mass of the Moon, L_m is the Earth–Moon distance and φ is the LP. The modification is in the scale of $M_m L_{PP}{}^2/ML_m{}^2$ or 0.01% for $L_{PP} = 6.0$ and $L_m = 60.0$, and is thus negligible. This indicates that variations in L_{PP} must be due to perturbations in Ω in the ZPF theory.

For example, perturbations in Ω will result in changes in L_{PP} that are given to first order by $\Delta L_{PP} = -2/3(2GM/3R_E{}^3)^{1/3}\Omega^{-5/3}\Delta\Omega = -2/3 L_{PP}(\Delta\Omega/\Omega)$. Assuming a steady axisymmetric magnetic field strength near the plasmapause and ideal magnetohydrodynamics, we have $\Delta\Omega/\Omega = \Delta E_r/E_r$. Finally, we get $\Delta L_{PP} = -2/3 L_{PP}(\Delta E_r/E_r)$, where E_r is the radial component of electric field and is the sum of $\mathbf{E}_{coro}$ and $\mathbf{E}_{conv}$. Applying the observed ΔE_r in Fig. 3d, the modelled perturbations of the plasmapause positions are shown in Fig. 3e.

Another model is based on LCE theory, which is suggested to be used under quiet or quasi-static geomagnetic conditions[30], an electric field model consisting of curl-free $\mathbf{E}_{coro}$ and $\mathbf{E}_{conv}$ (Kp = 3) components and perturbation of the electric field. Here the observed tidal disturbance electric field ΔE_r, which is a function of LP, is superimposed onto the convection-corotation electric field by changing $\mathbf{E}_{coro}$. We introduced an adjustable factor (f) and a linear scaling function $w(L)$ for low L values ($3 < L < 3.2$) to define a model for the corotation potential:

$$\Phi_{C1}(L) = \Phi_C(L) \times \left[1 - w(L) + w(L)/\left(1 + f\Delta E_r/\bar{E}_r\right)\right]$$

where

$$w(L) \begin{cases} 0, & L \leq L_0 \\ (L - L_0)/(L_1 - L_0), & L_0 < L < L_1 \\ 1, & L > L_1 \end{cases}$$

and $\bar{E}_r$ is the mean of E_r, and the values of L_0 and L_1 are 3.0 and 3.2, respectively. Scanning the value of f in increments of 0.05, we find that the modelled ΔL_{PP} best matches the observed ΔL_{PP} when $f = 0.3$. The modelled perturbations of the plasmapause positions are shown in Fig. 3f. Under such conditions, when the electric potential distribution is deviated to get the E_r distribution, the mean value of ΔE_r is calculated to be 38% of the observed one between L values of 3 and 6.

The reasons for superimposing 38% ΔE_r (as opposed to 100%) under different LPs onto the convection-corotation electric field might

be as follows. (1) The amplitude of E_r is of the same order as the Van Allen Probes Electric Fields and Waves instrument measurement error, hence the amplitude might be not well determined. (2) The radial electric field measured by the Van Allen Probes satellites will in general overestimate the value at the equator, assuming equipotential field lines. The electric field data used in this study are selected for the region of $-15° <$ magnetic latitude $< 15°$. The error introduced by the magnetic latitude effect can be estimated based on the dipole magnetic field model. The maximum and average errors of off-equator observations are ~7% and ~2%, respectively. (3) The LCE model we have used here is a simplified and idealized model, which may qualitatively but not quantitatively describe the tidal phenomenon.

Validation of the observed tidal signal

To eliminate any interference and confirm the tidal signal in subsets of the data, we divided the dataset into two nearly equal subdatasets using different three methods: (1) by year, 1977–2006 (51%) versus 2007–2015 (49%); (2) by solar radio flux at 10.7 cm (F10.7), F10.7 ≤ 103 (50%) versus F10.7 > 103 (50%); and (3) by season, January–June (48%) versus July–December (52%). The 6 h smoothed results are each depicted in Extended Data Fig. 5, showing that the tidal signal can be distinguished in all the six subsets. Extended Data Figure 6 shows the non-smoothed results binned in 2 h windows in both MLT and LP, with corresponding two-dimensional discrete Fourier transform[39] amplitudes shown in Extended Data Fig. 7, confirming that the diurnal and monthly variations are dominant. These results not only eliminate the possibility of data anomalies, but also increase the credibility of our results.

Visualizations of the lunar tide in the plasmasphere

Supplementary Video 1 shows tidal changes at the plasmapause using the same observational data as in Fig. 2a (here the smoothing window is 12 h for a clearer display). In panel a, the dashed line represents the background plasmapause position from all the 50,778 crossings and the solid line shows the perturbed plasmapause locations for different LPs, while the red cross represents the centre of the high tide for different LPs. Panel b shows the perturbations of plasmapause positions as a function of MLT for different LPs. This video shows that the 'high tide' peak of the perturbations moves regularly with the LPs. Note that the plasmapause perturbations are multiplied by 40 here.

Data availability

The plasmapause database is publicly available at http://www.geophys.ac.cn/ArticleDataInfo.asp?MetaId=103. The CE-3 EUVC data are publicly available at http://www.clep.org.cn/n6189350/n6760313/index.html. The IMAGE EUV image data are publicly available at http://euv.lpl.arizona.edu/euv/. The Electric Fields and Waves data are available at http://www.space.umn.edu/rbspefw-data/. The LP data are calculated by the planetary ephemeris DE432, which was created by the Jet Propulsion Laboratory in 2014. Source Data are provided with this paper.

References

58. Mozer, F. S. Analyses of techniques for measuring DC and AC electric fields in the magnetosphere. *Space Sci. Rev.* **14**, 272–313 (1973).
59. Pedersen, A., Mozer, F. & Gustafsson, G. (1998) Electric Field Measurements in a Tenuous Plasma with Spherical Double Probes. In: Pfaff, R. F. et al. (eds) *Measurement Techniques in Space Plasmas: Fields*, Geophysical Monograph Series, vol. 103. American Geophysical Union, Washington, D.C., pp 1-11 https://doi.org/10.1002/9781118664391.ch1
60. Li, W. et al. Global distributions of suprathermal electrons observed on THEMIS and potential mechanisms for access into the plasmasphere. *J. Geophys. Res. Space Phys.* **115**, A00J10 (2010).

61. Cho, J. et al. New model fit functions of the plasmapause location determined using THEMIS observations during the ascending phase of Solar Cycle 24. *J. Geophys. Res. Space Phys.* **120**, 2877–2889 (2015).

62. Kurth, W. S. et al. Electron densities inferred from plasma wave spectra obtained by the Waves instrument on Van Allen Probes. *J. Geophys. Res. Space Phys.* **120**, 904–914 (2015).

63. Tsyganenko, N. A. & Sitnov, M. I. Magnetospheric configurations from a high-resolution data-based magnetic field model. *J. Geophys. Res. Space Phys.* **112**, A06225 (2007).

64. Alken, P. et al. International geomagnetic reference field: the thirteenth generation. *Earth Planets Space* **73**, 49 (2021).

65. Oya, H. et al. Plasma wave observation and sounder experiments (PWS) using the Akebono (EXOS-D) satellite. Instrumentation and initial results including discovery of the high altitude equatorial plasma turbulence. *J. Geomagn. Geoelectr.* **42**, 411–442 (1990).

66. Moldwin, M. B., Thomsen, M. F., Bame, S. J., McComas, D. & Reeves, G. D. The fine-scale structure of the outer plasmasphere. *J. Geophys. Res.* **100**, 8021–8029 (1995).

67. Goldstein, J. Identifying the plasmapause in IMAGE EUV data using IMAGE RPI in situ steep density gradients. *J. Geophys. Res.* **108**, 1147 (2003).

68. Darrouzet et al. Density structures inside the plasmasphere: cluster observations. *Ann. Geophys.* **22**, 2577–2585 (2004).

69. Wygant, J. R. et al. The electric field and waves instruments on the radiation belt storm probes mission. *Space Sci. Rev.* **179**, 183–220 (2013).

70. Califf, S. et al. Large-amplitude electric fields in the inner magnetosphere: Van Allen Probes observations of subauroral polarization streams. *J. Geophys. Res. Space Phys.* **121**, 5294–5306 (2016).

71. Zhang, D. et al. Observations of impulsive electric fields induced by interplanetary shock. *Geophys. Res. Lett.* **45**, 7287–7296 (2018).

72. Baumjohann, W. & Treumann, R. A. *Basic Space Plasma Physics* (Imperial College Press/World Scientific Publishing Co., 1996); https://doi.org/10.1142/p015

73. Stern, D. P. The motion of a proton in the equatorial magnetosphere. *J. Geophys. Res.* **80**, 595–599 (1975).

74. Volland, H. A semiempirical model of large-scale magnetospheric electric fields. *J. Geophys. Res.* **78**, 171–180 (1973).

Acknowledgements

Author contributions

Q.S. and W.L. conceived this study. C.X., F.H., Q.S., W.L., A.T., R.G., C.Y. and A.W.D. carried out the data analysis, interpretation and manuscript preparation. X.Z.Z., Y.W., I.J.R., V.A., E.V.M., J.L., Q.Z., S.F., Z.P., X.X.Z., T.W., H.W. and Z.Z. contributed to the data interpretation and paper preparation. All authors reviewed the paper.

Competing interests

The authors declare no competing interests.

Additional information

Extended data Extended data are available for this paper at https://doi.org/10.1038/s41567-022-01882-8.

Supplementary information The online version contains supplementary material available at https://doi.org/10.1038/s41567-022-01882-8.

Correspondence and requests for materials should be addressed to Quanqi Shi or Wenlong Liu.

Peer review information *Nature Physics* thanks Balázs Heilig, Yosuke Yamazaki and Joseph Lemaire for their contribution to the peer review of this work.

**Reprints and permissions information** is available at www.nature.com/reprints.
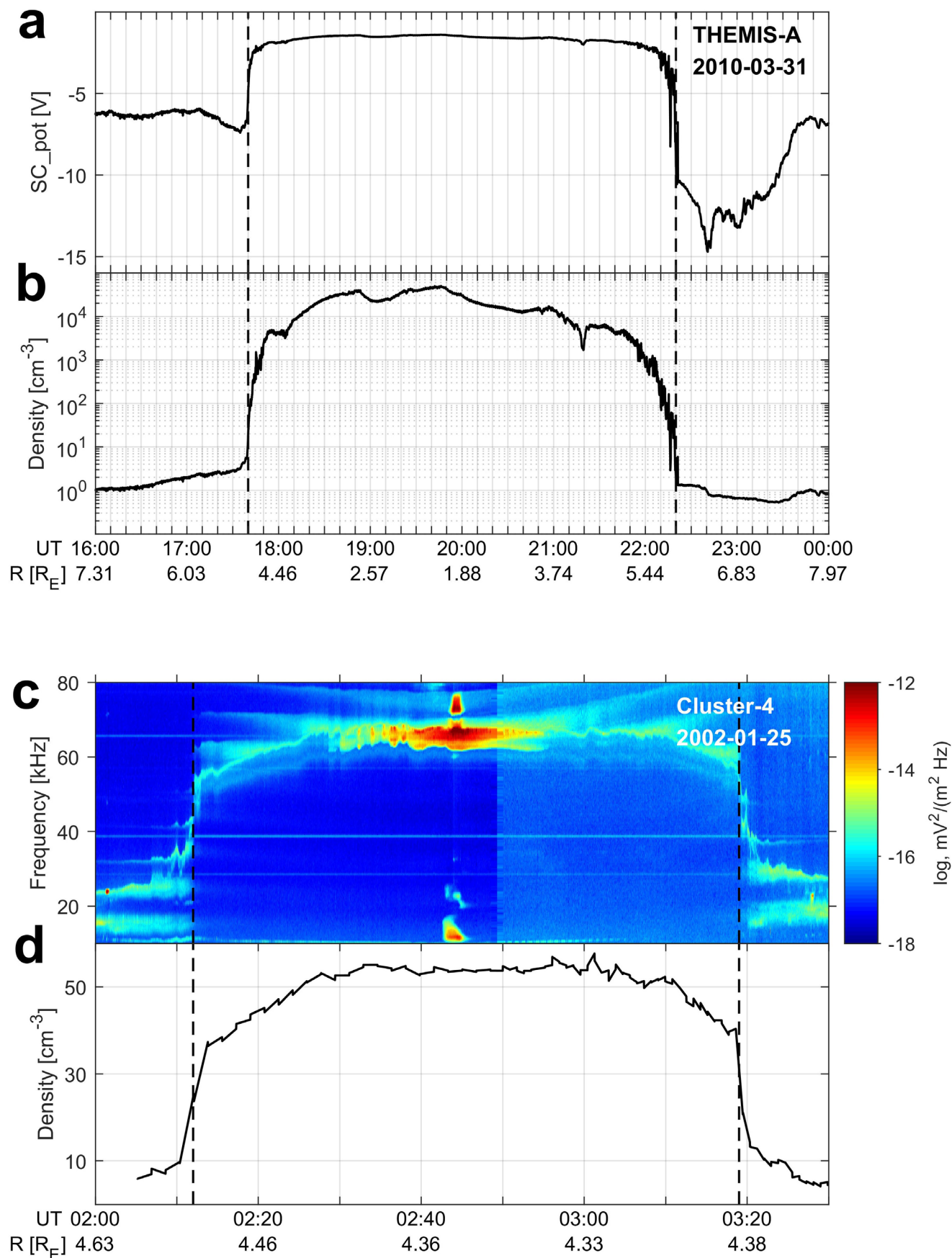
Extended Data Fig. 1 | Illustrations of plasmapause crossings using different types of plasmaspheric observations. a,b, The spacecraft potential and electron density measured by THEMIS-A on 31 March 2010. **c,d**, The spectrogram (the power spectral density of the electric field is indicated by the colour bars at the right of the panel) of the plasma wave measured by Cluster-4 and electron density deduced from the upper hybrid resonance frequency on 25 January 2002. The x-axis includes UT and radial distance of satellite in units of R_E ($1\,R_E$ = 6,371 km). The black vertical dashed lines mark the plasmapause position.
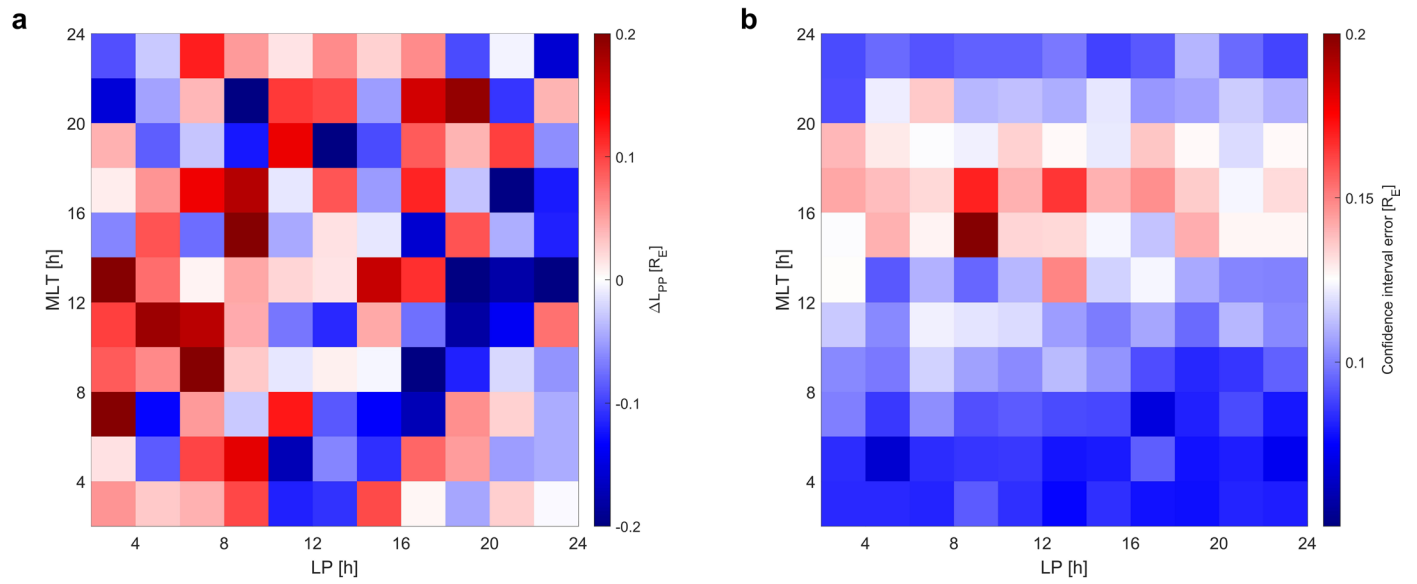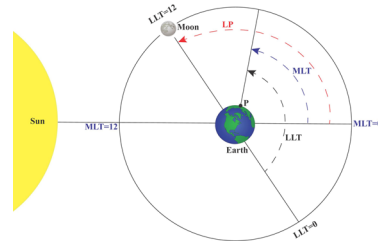
Extended Data Fig. 2 | Plasmapause location perturbations and corresponding errors. a, The distribution of perturbations of plasmapause position in units of R_E ($1\,R_E = 6{,}371$ km) in the MLT–LP frame. **b**, The corresponding 95% confidence interval error.
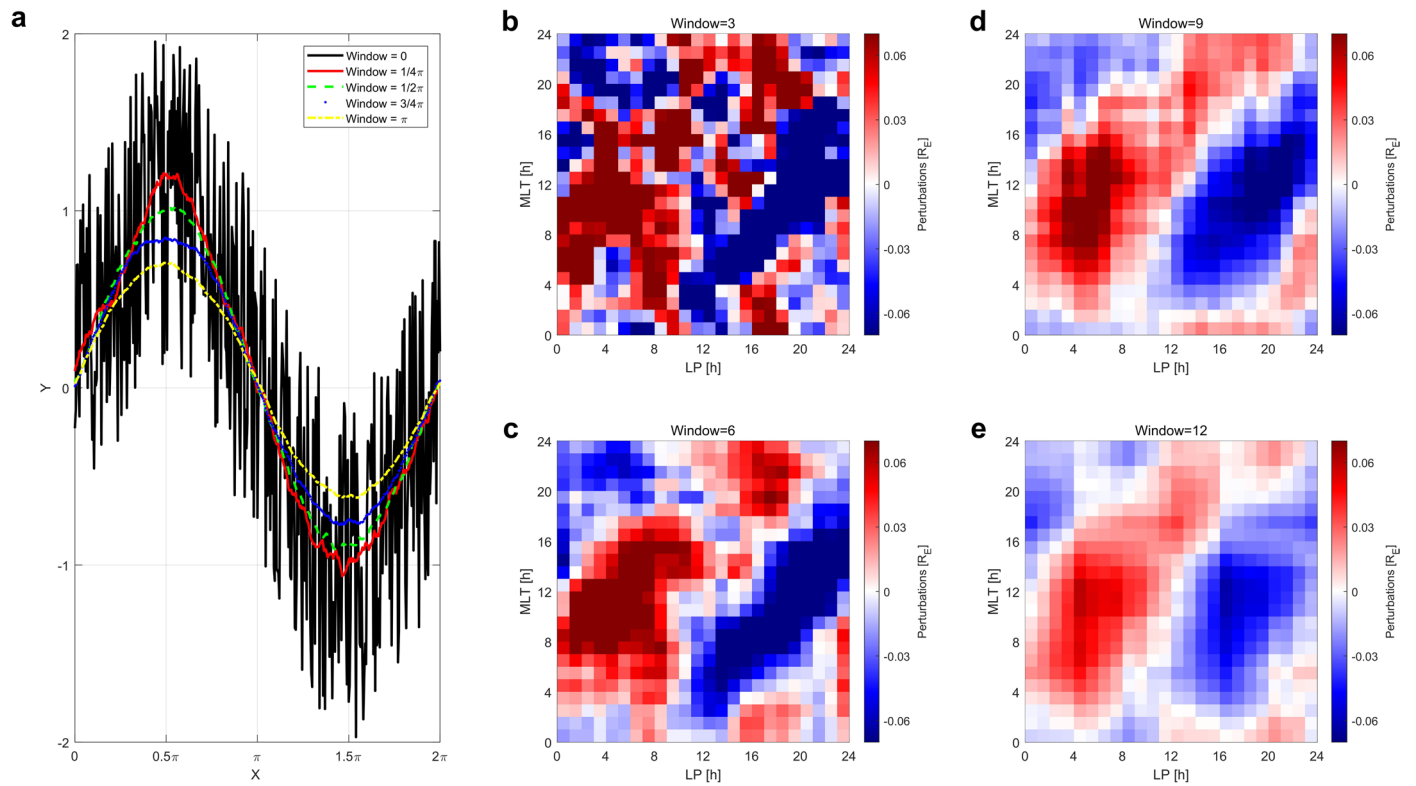
Extended Data Fig. 3 | Effect of a smoothing window on the periodicity of a dataset with a fixed period. a, An example ($y = \sin(x) + \mathrm{rand}(-1, 1)$; its period is 2π and the data with a period ($0 \leq X \leq 2\pi$) is shown here) with different smoothing windows. **b**–**e**, The distribution of perturbations of plasmapause position in units of R_E ($1\,R_E = 6{,}371\,\mathrm{km}$) in the MLT–LP frame with smoothing windows equal to 3, 6, 9 and 12 h, respectively.

Extended Data Fig. 4 | Definitions of the location frames. The MLT, LP, LLT and the relationship between them for a point P on the Earth.
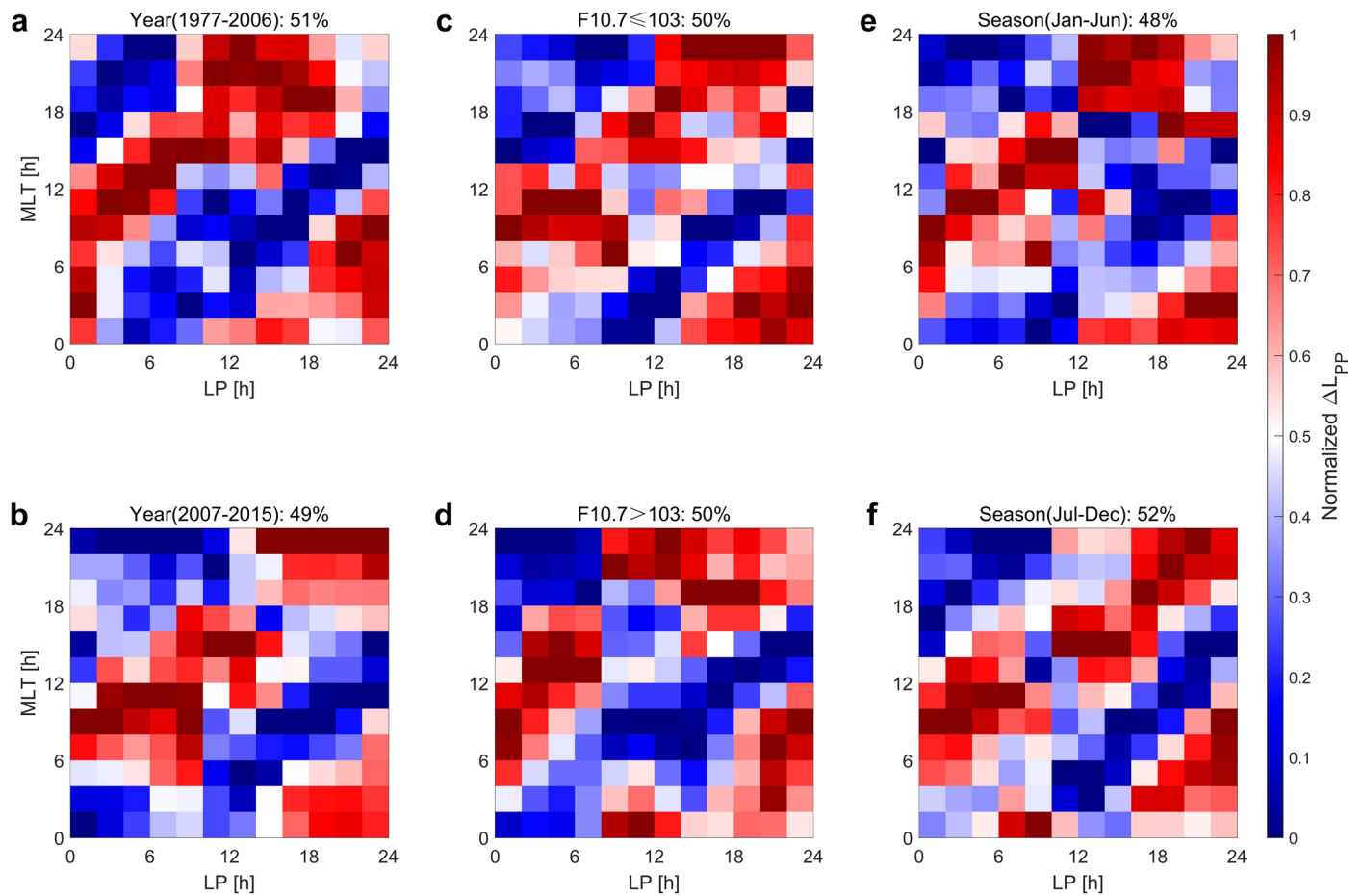
Extended Data Fig. 5 | Plasmapause perturbations binned in 6 h windows. The distribution of normalized perturbations of plasmapause positions (ΔL_{PP}) binned in 6 h windows in both MLT and LP, for these two parts equally divided by year (panels **a**,**b**), F10.7 (panels **c**,**d**) and season (panels **e**,**f**).
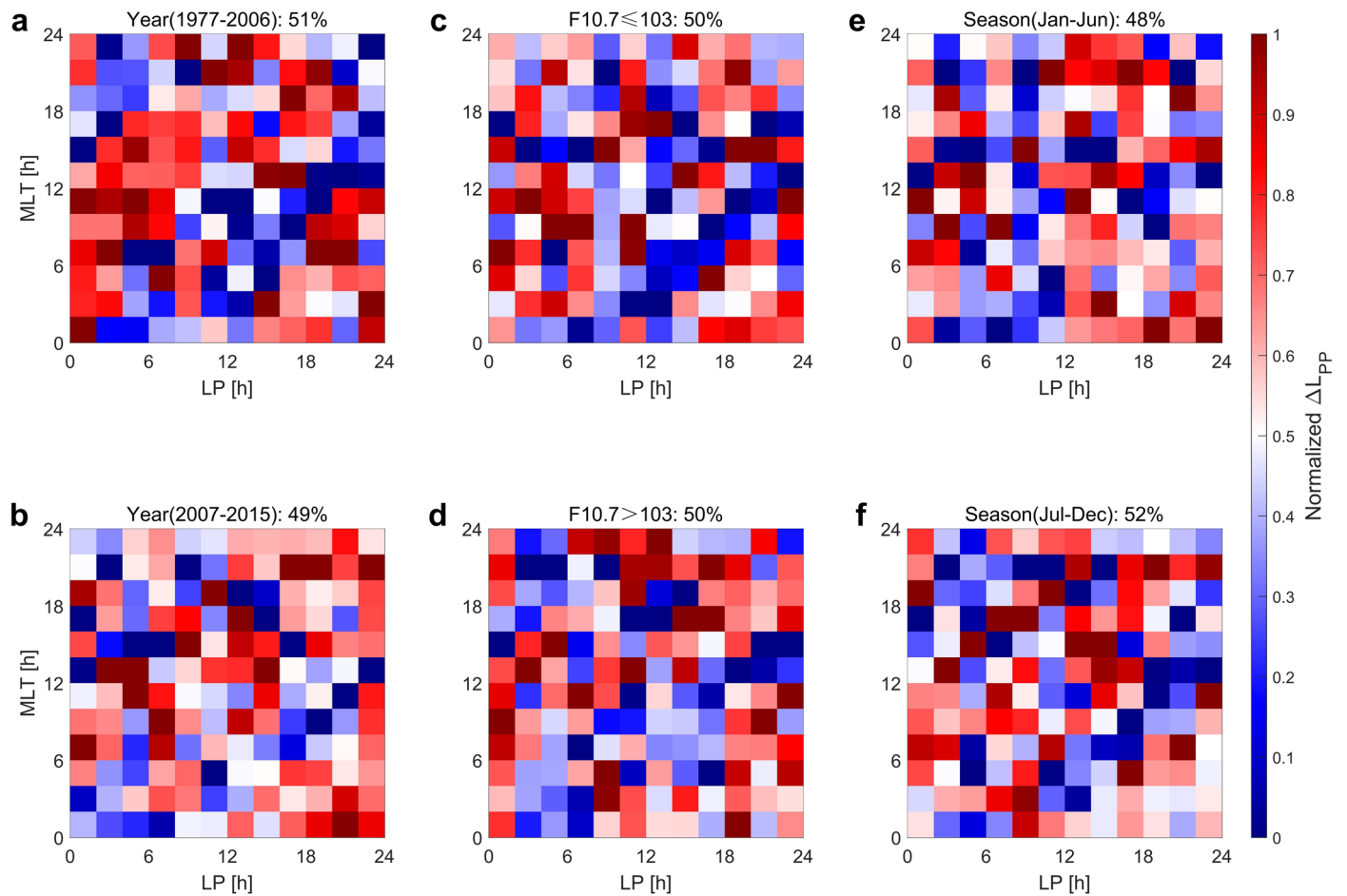
Extended Data Fig. 6 | Plasmapause perturbations binned in 2 h windows. The distribution of normalized perturbations of plasmapause positions (ΔL_{PP}) binned in 2 h windows in both MLT and LP, for these two parts equally divided by year (panels **a**,**b**), F10.7 (panels **c**,**d**) and season (panels **e**,**f**).
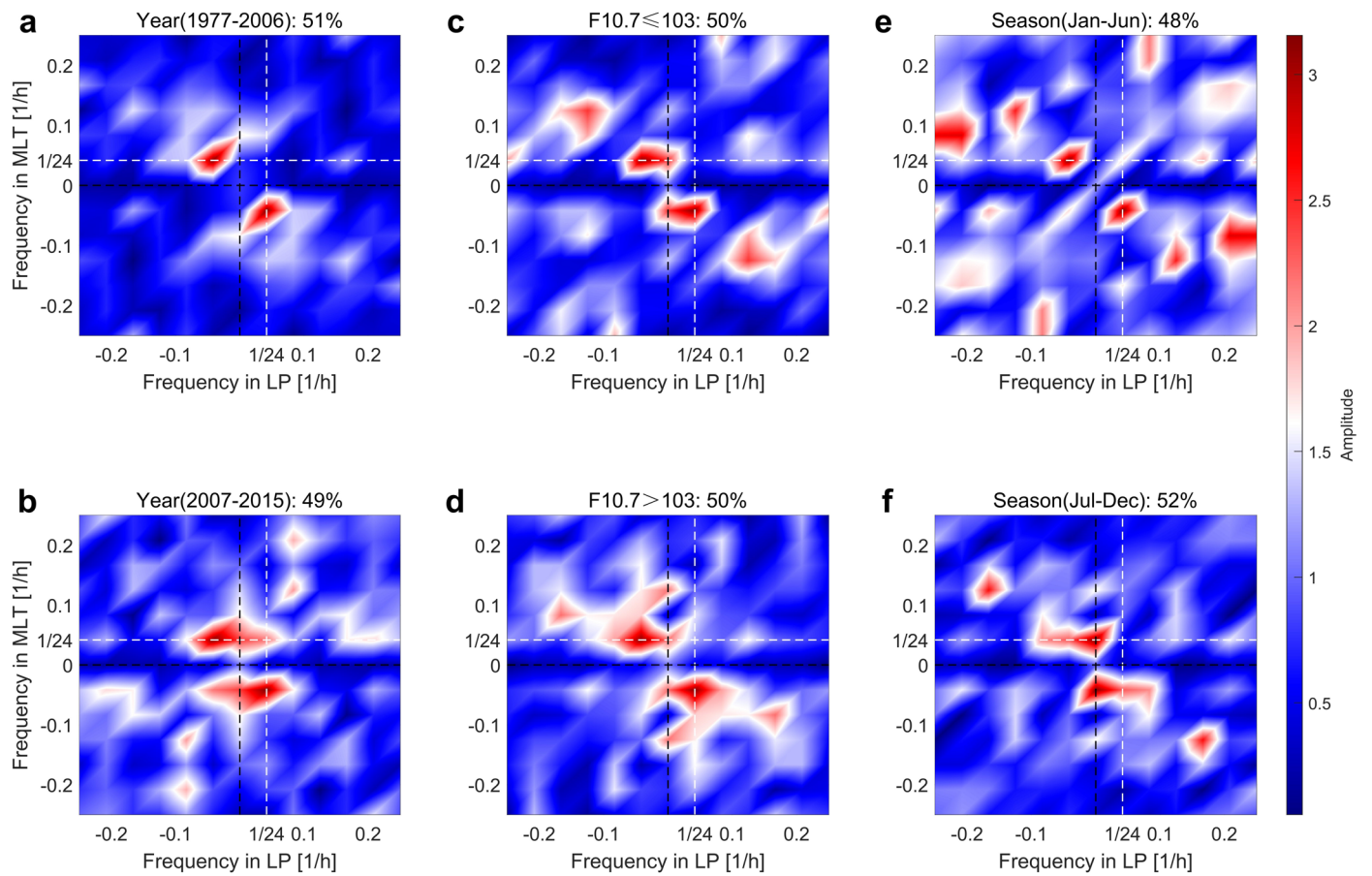
Extended Data Fig. 7 | Two-dimensional discrete Fourier transform amplitudes. The two-dimensional discrete Fourier transform amplitudes of normalized perturbations of plasmapause positions binned in 2 h windows in both MLT and LP, for these two parts equally divided by year (panels **a,b**), F10.7 (panels **c,d**) and season (panels **e,f**). The x-axis is frequency in LP and the y-axis is frequency in MLT. The black and white dashed lines indicate frequencies equal to 0 and 1/24 for reference, respectively.